

From a Fourier-Domain Perspective on Adversarial Examples to a Wiener Filter Defense for Semantic Segmentation

Nikhil Kapoor,¹ Andreas Bär,² Serin Varghese,¹
Jan David Schneider,¹ Fabian Hüger,¹ Peter Schlicht,¹ Tim Fingscheidt,²

¹ Volkswagen AG
Berliner Ring 2,
38440, Wolfsburg, Germany

² Technische Universität Braunschweig
Schleinitzstraße 22,
38106, Braunschweig, Germany

Abstract

Despite recent advancements, deep neural networks are not robust against adversarial perturbations. Many of the proposed adversarial defense approaches use computationally expensive training mechanisms that do not scale to complex real-world tasks such as semantic segmentation, and offer only marginal improvements. In addition, fundamental questions on the nature of adversarial perturbations and their relation to the network architecture are largely understudied. In this work, we study the adversarial problem from a *frequency domain perspective*. More specifically, we analyze discrete Fourier transform (DFT) spectra of several adversarial images and report two major findings: First, there exists a *strong connection between a model architecture and the nature of adversarial perturbations* that can be *observed and addressed in the frequency domain*. Second, the observed *frequency patterns are largely image- and attack-type independent*, which is *important for the practical impact of any defense making use of such patterns*. Motivated by these findings, we additionally propose an adversarial defense method based on the well-known Wiener filters that captures and suppresses adversarial frequencies in a data-driven manner. Our proposed method not only generalizes across unseen attacks but also beats five existing state-of-the-art methods across two models in a variety of attack settings.

1 INTRODUCTION

Szegedy *et al.* (Szegedy et al. 2014) pointed out that state-of-the-art machine learning models (Krizhevsky, Sutskever, and Hinton 2012; Chen et al. 2017; Löhdefink et al. 2019) can be easily fooled by adding carefully crafted adversarial perturbations to the input. Although these so-called adversarial examples are often imperceptible, they cause the model to make erroneous predictions with a high confidence (Nguyen, Yosinski, and Clune 2015). Since then, significant research efforts have been made in trying to get a deeper understanding into the existence of such adversarial attacks (Goodfellow, Shlens, and Szegedy 2015; Chakraborty et al. 2018), and in building reliable defense methods against such attacks (Bär et al. 2019, 2020; Klingner, Bär, and Fingscheidt 2020). Unfortunately, this problem is still far from solved.

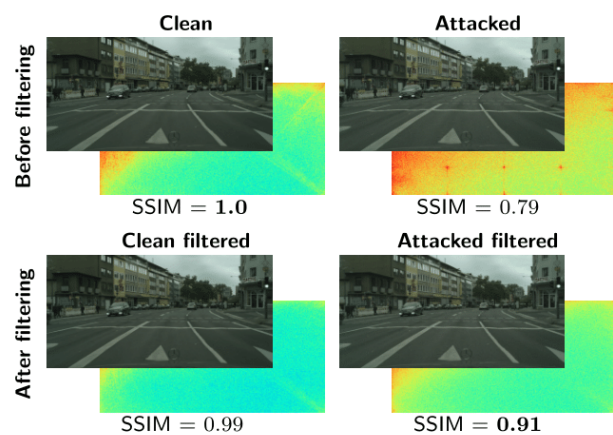


Figure 1: **Visualization of the effect of Wiener filtering** on clean data (left) and perturbed/attacked data (right). Foreground: Image data; Background: respective DFT spectrum. *Strong grid-shaped artifacts* are seen in the DFT spectrum of attacked images on ICNet (Zhao et al. 2018) (top right) which are suppressed after Wiener filtering (bottom right). Wiener filtering substantially improves the SSIM on attacked images (right side) and retains a reasonably high SSIM on clean images (left side).

Most existing defense methods are either computationally too expensive (Goodfellow, Shlens, and Szegedy 2015; Madry et al. 2018), provide a false sense of security (Papernot et al. 2016; Athalye, Carlini, and Wagner 2018), or offer only marginal improvements in a controlled setting (Guo et al. 2018; Shaham et al. 2018).

To obtain certifiable, effective, and low-complex defense methods, we need to shift our focus towards answering fundamental questions to improve our understanding of this adversarial robustness problem. For example, (Assion et al. 2019) made significant advancements in understanding adversarial attacks by proposing a structured taxonomy, specifying key components of an attack. In addition, (Yin et al. 2019) and (Wang et al. 2018, 2020a) analyzed the robust-

ness problem from a frequency-domain perspective to get a better understanding of trade-offs between robustness and performance and indicated that the lack of robustness is most likely correlated to a network’s sensitivity to high-frequency information in the input. Inspired from their work, we investigate adversarial attacks deeper in a frequency-domain formulation. Unlike existing analyses, we do this for a complex task, namely, semantic segmentation.

Our initial investigation revealed that *adversarial images tend to show strong artifacts in the frequency domain that are otherwise absent in their clean counterparts* (see Fig. 1). Further analysis with multiple attacks and models revealed two key findings: First, *the observed adversarial patterns in the frequency domain are largely image-and attack-type-independent*. Second, *there exists a strong connection between a model architecture and the nature of adversarial perturbations which can be observed and addressed in the frequency domain*.

Motivated by these findings, we propose a new adversarial defense method using the widely known Wiener filters (Scalart and Filho 1996; Kazubek 2003) from image and speech denoising domain. We argue that Wiener filters are suitable for adversarial image denoising, as these filters tend to remove adversarial noise from attacked images in the frequency domain, while at the same time, leaving clean images largely unaffected (see Fig. 1). In comparison to existing denoising methods (Buades, Coll, and Morel 2005; Dziugaite, Ghahramani, and Roy 2016; Xu, Evans, and Qi 2018; Aydemir, Temizel, and Temizel 2018), *Wiener filtering tends to outperform most of the methods in a variety of different attack settings*. In summary, our results indicate that Wiener filtering tends to have many favorable properties from an adversarial defense perspective. More specifically, *Wiener filter based denoising tends to generalize across unseen attack types and works even under varying attack settings* such as ϵ or L_p norm mismatch. We hypothesize that most of these properties are primarily because the frequency patterns that the Wiener filters try to suppress are already largely attack-type and attack-setting agnostic.

2 RELATED WORK

In this section, we discuss the related work on adversarial defense methods with a focus on denoising methods.

Adversarial Defenses: Most adversarial defenses fall into three categories: The first one is called *adversarial training* (Goodfellow, Shlens, and Szegedy 2015), which includes expensive retraining of the network on adversarial examples. Although successful, this does not easily scale to complex tasks and huge data sets (Kurakin, Goodfellow, and Bengio 2017). The second category is called *gradient masking* (Papernot et al. 2017), where the idea is to hide gradients from a potential hacker (Madry et al. 2018; Papernot et al. 2015; Cisse et al. 2017; Kannan, Kurakin, and Goodfellow 2018). However, (Athalye, Carlini, and Wagner 2018) showed that none of these approaches are truly effective, as the hacker can compute gradients using different models and still be successful.

Denoising-based Defenses: The third category is called

input transformations (Guo et al. 2018), where the main idea is to remove adversarial perturbations directly from the input before it is fed into the model. A few well-known methods of this type include image compression methods, such as JPEG (Dziugaite, Ghahramani, and Roy 2016) and JPEG2000 (Aydemir, Temizel, and Temizel 2018) compression, and various smoothing methods that reduce the feature space of the input, such as non-local (NL) means (Buades, Coll, and Morel 2005), bit-depth reduction (Xu, Evans, and Qi 2018) and median smoothing (Xu, Evans, and Qi 2018). Other interesting approaches include non-differentiable smoothing methods, such as quilting and total variance minimization (Guo et al. 2018), image cropping (Graese, Rozsa, and Boulton 2016), different forms of randomness (Xie et al. 2018; Cohen, Rosenfeld, and Kolter 2019; Raff et al. 2019), basis function transforms (Shaham et al. 2018), and more advanced methods, such as high-level guided denoiser (Liao et al. 2018) and BlurNet (Raju and Lipasti 2019).

In this work, we propose to use Wiener filters as an *input transformation* defense method that performs denoising in the frequency domain rather than in the spatial domain. For the state-of-the-art comparison, we limit our investigations to *spatial-domain based denoising methods that do not need additional retraining*. We choose five such methods that are often cited in the defense literature (Xu, Evans, and Qi 2018; Shaham et al. 2018; Das et al. 2018; Tang, Fan, and Yezzi 2019) including two image compression methods, namely JPEG (Dziugaite, Ghahramani, and Roy 2016) and JPEG2000 (Aydemir, Temizel, and Temizel 2018) compression and three feature squeezing smoothing methods, namely median blurring (Xu, Evans, and Qi 2018), non-local (NL) means (Buades, Coll, and Morel 2005) smoothing, and bit-depth reduction (Xu, Evans, and Qi 2018).

3 WIENER FILTER AS ADVERSARIAL DEFENSE

Wiener filters are widely used as denoising filters in traditional signal processing (Smith 2003; Burger and Burge 2008; Petrou and Petrou 2010). In this section, we introduce an adaptation of the Wiener filter as an adversarial defense which is achieved by estimating the power spectrum of the underlying adversarial perturbations in the frequency domain. But first, we introduce some mathematical notation.

3.1 Mathematical Notations

Let $\mathbf{x} \in \mathbb{G}^{H \times W \times C}$ be an image in the spatial domain with height H , width W , $C = 3$ color channels, set of integer gray values \mathbb{G} , and $\mathbf{x} \in \mathcal{X}$, where \mathcal{X} represents a dataset. In the frequency domain, we define $\mathbf{X} = (X_{k,\ell,m}) \in \mathbb{C}^{H \times W \times C}$, with $X_{k,\ell,m}$ being the element of \mathbf{X} at frequency coordinates k, ℓ, m along height, width, and color channels, respectively, and \mathbb{C} denoting the set of complex-valued numbers. Further, \mathbf{X} is obtained by computing the 3D discrete Fourier transform (DFT) following (Gonzalez

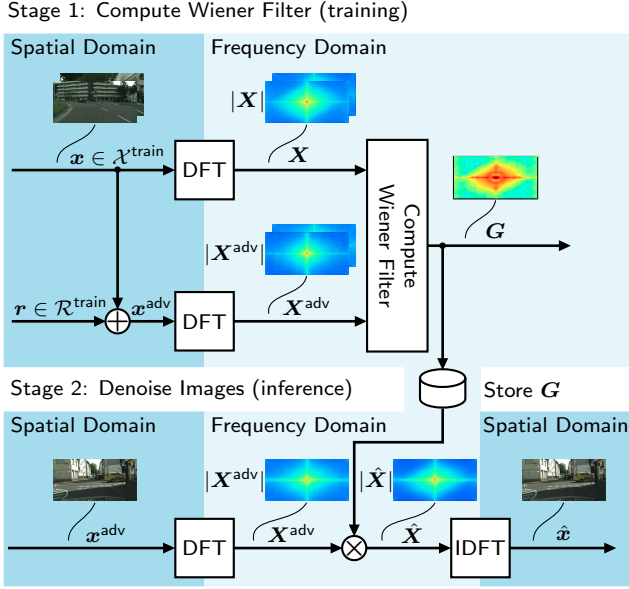


Figure 2: **Method Overview.** In **stage 1**, a Wiener filter is computed in the frequency domain using a paired set of images $\mathbf{x} \in \mathcal{X}^{\text{train}}$ taken from the training set $\mathcal{X}^{\text{train}}$ with their respective adversarial perturbations \mathbf{r} or rather their adversarial images \mathbf{x}^{adv} . In **stage 2**, during inference, the Wiener filter \mathbf{G} is applied as an input preprocessing step such that it suppresses adversarial frequencies (if present) in the frequency domain leading to a denoised image $\hat{\mathbf{x}}$ in the spatial domain after an inverse DFT.

and Woods 2002) as

$$X_{k,\ell,m} = \sum_{h=0}^{H-1} \sum_{w=0}^{W-1} \sum_{c=0}^{C-1} x_{h,w,c} e^{-j2\pi(\frac{k}{H}h + \frac{\ell}{W}w + \frac{m}{C}c)}, \quad (1)$$

where, similarly to the frequency domain, $x_{h,w,c}$ are the elements of \mathbf{x} at spatial coordinates h, w, c in height, width and color channels, respectively. For the sake of simplicity, we denote the 3D DFT with the notation $\mathbf{X} = \mathcal{F}(\mathbf{x})$. Similarly, the 3D inverse DFT is denoted as $\mathbf{x} = \mathcal{F}^{-1}(\mathbf{X})$. For the sake of completeness, the 3D inverse DFT following (Gonzalez and Woods 2002) is defined as

$$x_{h,w,c} = \frac{1}{HWC} \sum_{k=0}^{H-1} \sum_{\ell=0}^{W-1} \sum_{m=0}^{C-1} X_{k,\ell,m} e^{j2\pi(\frac{k}{H}h + \frac{\ell}{W}w + \frac{m}{C}c)}. \quad (2)$$

The image \mathbf{x} is fed as an input to a semantic segmentation neural network $\mathfrak{F}(\cdot)$ having network parameters θ and output $\mathbf{y} = \mathfrak{F}(\mathbf{x}, \theta) \in [0, 1]^{H \times W \times |\mathcal{S}|}$, with the set of classes \mathcal{S} , and $|\mathcal{S}|$ being the number of classes. Each element of \mathbf{y} is considered to be a posterior probability $y_{i,s} = P(s|i, \mathbf{x})$ for the class $s \in \mathcal{S}$ at pixel index $i \in \mathcal{I} = \{1, 2, \dots, H \cdot W\}$.

An adversarial attack comprises the computation of an adversarial perturbation $\mathbf{r} \in \mathbb{R}^{H \times W \times C}$, such that $\|\mathbf{r}\|_p \leq \epsilon$, with $\epsilon \in \mathbb{R}^+$ defined as an imperceptibility constraint based on the L_p norm, denoted by $\|\cdot\|_p$. Further, an adversarial

example is defined as

$$\mathbf{x}^{\text{adv}} = \mathbf{x} + \mathbf{r}. \quad (3)$$

These adversarial perturbations \mathbf{r} can be computed for multiple images individually, creating a set \mathcal{R} of adversarial perturbations with $\mathbf{r} \in \mathcal{R}$.

3.2 Defense Objective

In the absence of an adversarial attack detector, we aim at designing a denoising filter that removes an adversarial perturbation \mathbf{r} from an adversarial image \mathbf{x}^{adv} , and at the same time to the largest extent preserves the clean image \mathbf{x} . Mathematically speaking, if our denoising function is denoted by $g(\cdot) : \mathbb{G}^{H \times W \times C} \rightarrow \mathbb{G}^{H \times W \times C}$, then ideally, the objective of denoising can be defined as

$$\forall \mathbf{x}, \mathbf{x}^{\text{adv}} : g(\mathbf{x}) = \mathbf{x} \wedge g(\mathbf{x}^{\text{adv}}) = \mathbf{x}. \quad (4)$$

A denoising function that satisfies the abovementioned properties has direct applications as an input preprocessing step during inference. Since the function $g(\cdot)$ will not alter a clean image \mathbf{x} significantly, in contrast to an adversarial image \mathbf{x}^{adv} , we do not need to detect whether the input image is adversarial or not. In addition, we also do not want the original baseline performance on clean filtered images to suffer too much.

3.3 Wiener Filter

Wiener filters (Wiener 1949) are used primarily as a denoising technique in traditional signal processing both for vision (Kazubek 2003; Kethwas and Jharia 2015) and speech (Fingscheidt, Suhadi, and Stan 2008; Suhadi, Last, and Fingscheidt 2011; Meyer, Elshamy, and Fingscheidt 2020). These filters typically operate in the frequency domain and assume that the spectral properties of the original images as well as the noise are known or can be estimated.

In the context of adversarial attacks, we consider the clean images \mathbf{x} as the original signal, which is corrupted by additive noise (also called adversarial perturbations \mathbf{r}) giving a degraded output image \mathbf{x}^{adv} . In the DFT domain, (3) can be written as

$$\mathcal{F}(\mathbf{x}^{\text{adv}}) = \mathcal{F}(\mathbf{x}) + \mathcal{F}(\mathbf{r}), \quad (5)$$

where $\mathcal{F}(\cdot)$ is the 3D DFT computed from (1). A Wiener filter in the DFT domain typically results in a transfer function $\mathbf{G} \in [0, 1]^{H \times W \times C}$, such that the mean squared error between the estimated image in the DFT domain $\hat{\mathbf{X}}$ and the original clean image \mathbf{X} is minimized (Gonzalez and Woods 2002). The following assumptions are made in the DFT domain: The perturbation $\mathbf{R} = \mathcal{F}(\mathbf{r})$ and the image \mathbf{X} are uncorrelated (can be assumed due to their transferability (Demontis et al. 2019)), zero mean, and the pixel values in the estimate $\hat{\mathbf{X}}$ are a linear function of the pixel values in the degraded image \mathbf{X}^{adv} . Based on these assumptions, the Wiener filter transfer function \mathbf{G} in the DFT domain is computed by

$$G_{k,\ell,m} = \frac{|X_{k,\ell,m}|^2}{|X_{k,\ell,m}|^2 + |R_{k,\ell,m}|^2}, \quad (6)$$

where $G_{k,\ell,m}$ refers to the elements of \mathbf{G} at frequency coordinates k, ℓ, m respectively, and $|X_{k,\ell,m}|^2, |R_{k,\ell,m}|^2$ refer

to the power spectrum of the clean image and the additive noise, respectively. Given this filter, one could compute the denoised image in the DFT domain by

$$\hat{\mathbf{X}} = \mathbf{G} \odot \mathbf{X}^{\text{adv}}, \quad (7)$$

where \odot represents an element-wise multiplication. Finally, the denoised image in the spatial domain could be recovered by simply computing the inverse DFT (IDFT) as in (2):

$$\hat{\mathbf{x}} = \mathcal{F}^{-1}(\hat{\mathbf{X}}). \quad (8)$$

The challenge in real-world denoising applications is now to estimate the clean signal power spectrum and the noise power spectrum, or, alternatively, the signal-to-noise ratio $SNR_{k,\ell,m} = |X_{k,\ell,m}|^2 / |R_{k,\ell,m}|^2$, allowing (6) to be rewritten as

$$G_{k,\ell,m} = \frac{SNR_{k,\ell,m}}{1 + SNR_{k,\ell,m}}. \quad (9)$$

For our application, we can state that the filter defined in (6) optimally works for a single known image and known noise. In an experimental setting, where $X_{k,\ell,m}$ and $R_{k,\ell,m}$ are available separately, one can compute (6) and apply (7) and (2) to achieve an *upper performance limit* later on. For a real-world input transformation, however, we adapt this to unknown images in inference for an attack type a , by simply taking the arithmetic mean over multiple images from a training set $\mathbf{x} \in \mathcal{X}^{\text{train}} = \mathcal{X}$ as follows

$$G_{k,\ell,m}^{(a)} = \frac{1}{|\mathcal{X}|} \sum_{\mathbf{x} \in \mathcal{X}} \frac{SNR_{k,\ell,m}^{(a)}}{1 + SNR_{k,\ell,m}^{(a)}}, \quad (10)$$

with the superscript a referring to the respective attack type used for creating the perturbation $R_{k,\ell,m}^{(a)}$ to obtain $SNR_{k,\ell,m}^{(a)} = |X_{k,\ell,m}|^2 / |R_{k,\ell,m}^{(a)}|^2$, and then to obtain the single-attack Wiener filter $G_{k,\ell,m}^{(a)}$, or $\mathbf{G}^{(a)}$. This averaging approach is indeed novel and ambitious for combating adversarial perturbations, as it requires a similar SNR for different images at a particular DFT bin for a certain attack type a , as we will show in Section 5. Similarly, we can even combine filters from multiple attack types $a \in \mathcal{A}$ from a set of attacks \mathcal{A} to obtain a single Wiener filter $\mathbf{G}^{(\mathcal{A})}$ with coefficients

$$G_{k,\ell,m}^{(\mathcal{A})} = \frac{1}{|\mathcal{A}|} \sum_{a \in \mathcal{A}} G_{k,\ell,m}^{(a)}. \quad (11)$$

Note that this Wiener filter computation is novel as well and even more ambitious, as the aforementioned assumptions leading to (10) are augmented by the assumption that the similar SNR even holds for different attack types. In other words, we expect $SNR_{k,\ell,m}^{(a)}$ for a certain network topology to be similar for various attack types $a \in \mathcal{A}$.

4 EXPERIMENTAL SETUP

In this section, we describe the most important details of our experimental setup. More details can be found in the supplementary material.

Table 1: **Attack parameters** used in this work.

Attack	Target	Parameter	Epsilon ϵ		Iterations
			L_∞	L_2	
mFGSM	Car	$\mu = 10$	5, 10	5000	20
	Pedestrian		5, 10	-	20
Metzen	Car	-	5, 10, 40	-	20
	Pedestrian	-	5, 10, 40	-	20
I.M.	-	-	5, 10, 40	-	20
Mopuri	-	$\mu = 1$ $\ell = \text{"conv3"}$	5, 10	-	20

Table 2: **Method parameters** used in this work.

Method	Parameters
JPEG (Roy et al. 2016)	Quality = 90
JPEG2000 (Aydemir et al. 2018)	Quality = 400
NL Means (Buades et al. 2005)	Search Window=13x13, Size=3x3, Strength=2
Median Blur (Xu et al. 2017)	Filter Size = 3×3
Bit-Depth Reduction (Xu et al. 2017)	Bits = 5

4.1 Employed Datasets and Models

We perform our experiments on a well-known publicly available data set for semantic segmentation, namely Cityscapes (Cordts et al. 2016). This data set consists of 5000 RGB images with resolution 2048×1024 of urban street scenes from different cities across Germany. The data split comprises 2975 training images, 500 validation images, and 1525 test images. We report our results on the clean and adversarially perturbed Cityscapes validation set using the (mean) intersection over union (IoU).

Regarding models, we focus on two well-known semantic segmentation models, namely FCN (Long, Shelhamer, and Darrell 2015) and ICNet (Zhao et al. 2018). The FCN employs fully convolutional layers and is considered as one of the pioneer architectures for semantic segmentation inspiring many future works (Zhang et al. 2018; Chen et al. 2015; Yu and Koltun 2016; Chen et al. 2018). For our work, we trained the FCN-VGG16 variant from scratch on the Cityscapes dataset for 120 epochs with a learning rate of 0.0001 and batch size 4 using two Nvidia GTX 1080Ti GPUs and achieved 48.48% mIoU on the validation set.

On the other hand, the ICNet model (Zhao et al. 2018) employs a multi-stream architecture which is capable of real-time inference at 30 fps. The architecture employs cascade image inputs (i.e. low, medium and high resolution) with separate streams for each resolution combined with a feature fusion unit that outputs a full resolution segmentation map. For our work, we use an openly available pre-trained Tensorflow implementation (Yang 2017) of the ICNet that achieves 67.25% mIoU on the validation set.

4.2 Adversarial Attacks

We employ four kinds of adversarial attacks for semantic segmentation; two targeted attacks, namely Metzen LLM (Metzen et al. 2017) and Momentum FGSM (mFGSM) (Dong et al. 2018); one untargeted attack, namely Data-Free Mopuri (Reddy, Ganeshan, and Babu 2018); and one confusion-based attack, namely Iterative Mirror (Metzen et al. 2017). These attacks are adopted from the AidKit¹ attack framework proposed by (Assion et al. 2019) and first tested in a *gray-box setting*. The attack parameters used in this work are shown in Fig. 1 (see supplementary material for further details on all attacks).

Backward Pass Differential Approximation (BPDA): (Athalye, Carlini, and Wagner 2018) proposed the BPDA algorithm to generate adversarial examples for pre-processing based defenses that are either hard or impossible to differentiate. Following (Shaham et al. 2018), we test BPDA using mFGSM attack on all the defense methods considered in this work. For each defense method separately, we report the attack success, i.e., mIoU on attacked images computed over the validation set. For the sake of fair comparison, we keep the attack parameters fixed for each defense method, i.e., $\epsilon = 10$ for an L_∞ norm using $T = 20$ iteration steps.

4.3 Baseline Defenses

For each baseline method, we use the best parameter settings found either from literature (Xu, Evans, and Qi 2018) or by using a line search algorithm, as reported in Tab. 2.

5 EXPERIMENTAL RESULTS

In this section, we discuss two kinds of experiments. First, we evaluate adversarial examples in the frequency domain and report our findings and observations. Second, we perform an in-depth evaluation of the Wiener filters as an adversarial defense method and compare it to existing methods.

5.1 Experiments with Fourier-Domain Analyses

We investigate adversarial images in the frequency domain and compare it to their clean counterparts. First, we visualized the amplitude spectrum of a *single* sample clean image and its corresponding attacked image (using mFGSM attack computed on the ICNet model with an L_∞ norm and $\epsilon = 10$) in Fig. 1. We observed that there exist *several periodic grid-shaped artifacts* in the *frequency domain of attacked images* which were absent in its clean counterparts.

Intrigued by these artifacts, we visualized the averaged DFT spectra over all 2975 training set images for adversarial perturbations computed using the same mFGSM attack and show the results in Fig. 3 a) (top left). Surprisingly, we found that *every single attacked image had more or less the exact same grid-shaped artifacts in the frequency domain*. We then performed a series of carefully designed ablation experiments to investigate the source of these artifacts.

Effect of attack strength and iterations. We investigate the effect of varying attack strength $\epsilon \in [5, 10, 15, 20]$ and number of iterations $T \in [10, 20, 30, 50]$, on the artifacts.

Our results indicate that the *grid-patterns are largely independent of the chosen attack parameters* with only small variations in artifact severity (see supplementary material).

Effect of attack type. So far, we limited our investigations to a single attack type, i.e. mFGSM. We now study different attacks (see Tab.1) and visualize the corresponding averaged amplitude spectra for the same 2975 training images (results shown in Fig. 3 a) (top row)). Note that these attacks have fundamentally different optimization goals (i.e. targeted, untargeted or confusion) and even different optimization techniques. However, *even with these fundamental differences in the attack types, the same grid-shaped artifact was observed across all images for all attacks*.

Effect of network architecture. So far, we found that *adversarial attacks tend to share inherent similarities, observed via artifacts in the frequency domain*. These artifacts are also largely *image-type and attack-configuration independent*. Next, we investigate the FCN architecture and again perform similar experiments. From the results shown in Fig. 3 a) (bottom row), a *box-shaped artifact* was observed instead. These artifacts, like before, also remained consistent across several images and attacks (see supplementary material). Hence, since different architectures lead to different artifacts, it seems that *the artifacts seem to have a strong connection to the underlying network architecture*.

Effect of varying layers in Mopuri attack. In the attack generation process, unlike the mFGSM, Metzen, and I.M. attacks, which need gradients to be processed through the entire network architecture, the Mopuri attack, by design, only needs gradients from a subset of layers. We investigate the effect of varying layers ℓ for Mopuri attack and visualize the average amplitude spectra in Fig. 4. Surprisingly this time, *we observed clear variations in the grid-shaped artifacts by varying the underlying layers*. This finding further reaffirms our earlier hypothesis on the connection of the network architecture and its corresponding artifacts. Interestingly, the artifacts of Mopuri (attacked on last layer `conv6`) are similar to artifacts emerging out of all the remaining attacks. This is mainly because, in this case, for all attacks, the number of layers used for gradient computation remains the same.

5.2 Discussion about artifacts

From our initial set of experiments, it is evident that certain parts of a network, more specifically the layers, lead to several artifacts in the frequency domain of adversarial images. Although the type of artifacts might vary across network architectures, they tend to remain consistent across different attack settings and attack types. From the literature, we find two possible reasons for these artifacts.

Downsampling and aliasing. Traditional signal processing literature (Lyons and Fugal 2014) illustrates that incorrect downsampling i.e., one where the sampling frequency does not satisfy the Nyquist-Shannon sampling criteria (Gazi 2018), leads to aliasing artifacts resulting in periodic grid points in the frequency domain.

Upsampling and checkerboard patterns. At the same time, upsampling layers or deconvolutional operations also lead to periodic patterns in the frequency domain, commonly known as checkerboard artifacts (Odena, Dumoulin,

¹<https://aidkit.ai/>

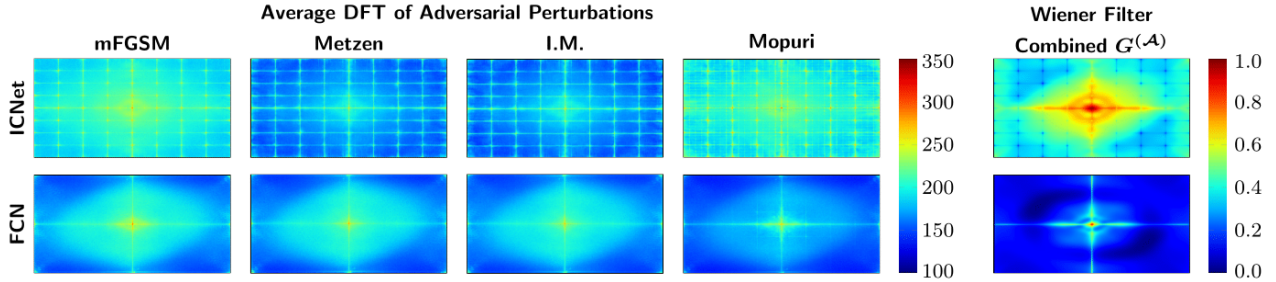


Figure 3: **Visualization of a) average amplitude spectra of adversarial perturbations and b) the corresponding combined Wiener filter $G^{(A)}$ (11) for ICNet and FCN.** For each adversarial attack, we estimate $\mathbb{E}[|\mathcal{F}(x^{\text{adv}} - x)|]$ over the entire 2975 Cityscapes training set images. The DFT spectra are log-scaled such that low-frequency points are at the center of the images.

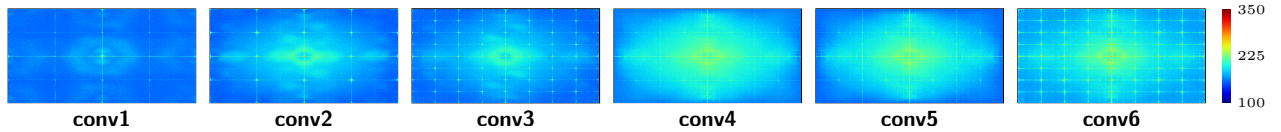


Figure 4: **Visualization of average amplitude spectra of adversarial perturbations** computed for the Mopuri attack on the ICNet model varied along attacked layer ℓ . We estimate $\mathbb{E}[|\mathcal{F}(x^{\text{adv}} - x)|]$ for 100 randomly chosen training set images.

and Olah 2016). Similar observations were found by (Frank et al. 2020) and (Wang et al. 2020b) in images generated by generative adversarial networks (GAN’s).

Artifacts and adversarial examples. For these above-mentioned reasons, we hypothesize that the artifacts we observed in adversarial images are also most likely due to different upsampling and downsampling operations in the network. These artifacts arise during the attack generation process as gradients are passed across different layers of a network. Since most attacks propagate gradients through the same set of layers in a network, the underlying frequency patterns therefore remain consistently similar (as seen in Fig. 3). Specifically, in the ICNet, the grid-shaped artifacts are most likely due to its multi-stream setup with many upsampling and downsampling layers that are fused together at intermediate steps. These grid-shaped artifacts only get stronger as we move further in the network (Fig. 4). The FCN, on the other hand, has only a single stream with primarily downsampling layers leading to box-shaped artifacts.

5.3 Experiments with Defense Methods

Motivated by our findings from the first set of experiments, we now investigate the benefits of using Wiener filters as a defense for semantic segmentation. We present results on two variants of Wiener filters, i.e. WF (combined) or $G^{(A)}$ (11) (also visualized in Fig. 3 (right column)), a filter averaged across all six attacks, and WF (mFGSM) or $G^{(a)}$ (6), a single-attack filter where the attack type a corresponds to mFGSM attack. Additional variants of WF (epsilon mismatch) with detailed improvements across individual attack types can be found in the supplementary material.

Effect on SSIM and MSE. We investigate the denoising improvements using traditional metrics such as SSIM

and MSE for attacked images x^{adv} and attacked denoised image \hat{x} , both w.r.t. the original clean images x . Averaged results across six attack types (each attack computed with an L_∞ norm with $\epsilon = 10$) for the entire 500 images of the Cityscapes validation set is shown in Fig. 5 (a). These results indicate strong improvements with denoising using Wiener filters on SSIM and MSE which is significantly better than other baseline methods. WF (combined) achieves an impressive 5% average SSIM improvement with a corresponding 20 points decrease in MSE after denoising. At the same time, WF (mFGSM), although trained only on a single attack and tested across all 6 attacks (5 of which are unseen), still achieves an overall 5% average improvement in SSIM and 13 points decrease in MSE, indicating strong generalization properties of Wiener filters to unseen attacks. In contrast, most of the baseline methods (except NLM) barely improve the SSIM (on average +0.87%), and in fact lead to a higher MSE (on average +4.74 units) after denoising.

Effect on mIoU (L_∞ norm). We investigate the improvement in mean intersection-over-Union (mIoU) on all the methods and two models, namely ICNet (Zhao et al. 2018) and FCN (Long, Shelhamer, and Darrell 2015) (as described in Section 4). Once again, averaged results over all attacks and all validation set images are reported in Fig. 5 (b). For both models, attacks are computed based on L_∞ norm with attack strength as shown in Fig. 1. From the results, we observe that *WF consistently offers improvements better than almost all other baseline methods on both models (on average +6% absolute mIoU on ICNet and +3% absolute mIoU on FCN on all attacks)*. At the same time, the performance on clean images remains largely unaffected with only a 0.5% absolute decrease in mIoU. However, to our surprise WF (mFGSM) even surpasses WF (Combined) with an impres-

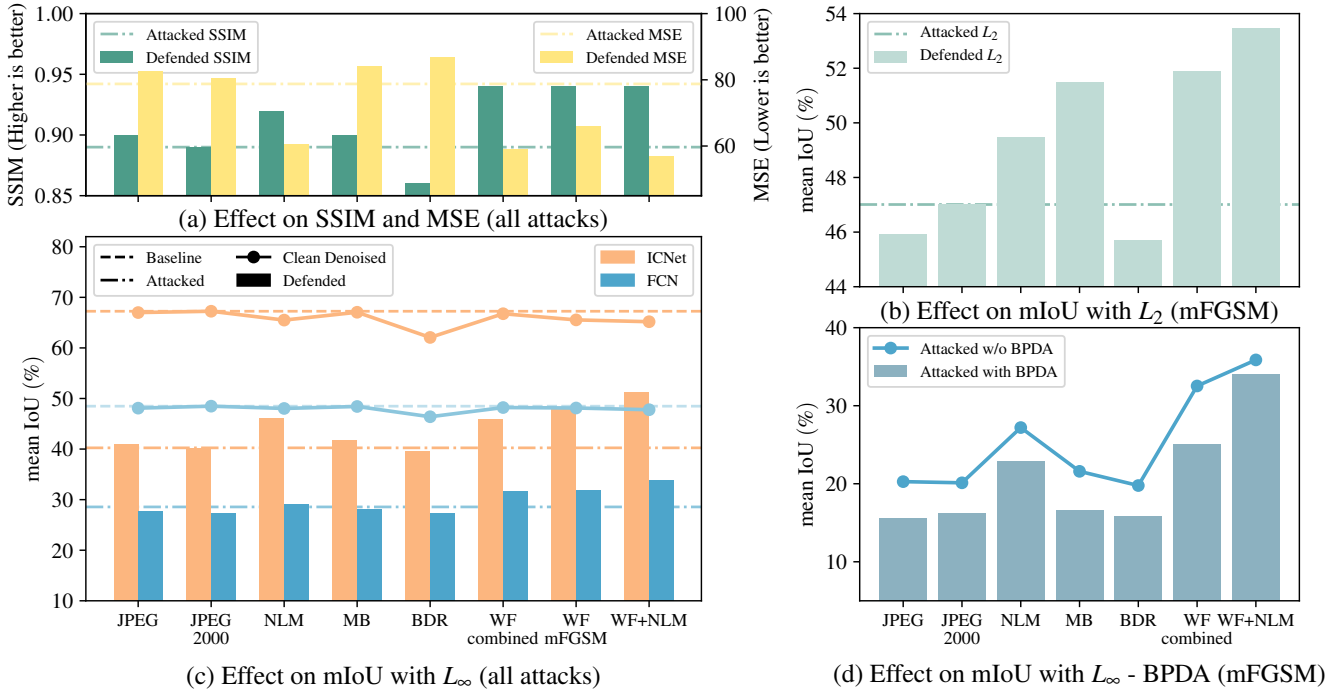


Figure 5: **Denoising Results of Wiener Filtering compared with existing state-of-the-art methods.** (a) Averaged SSIM and MSE improvement across all L_∞ based attacks on ICNet (Zhao et al. 2018), (b) Averaged mIoU improvement across all L_∞ based attacks for ICNet and FCN, (c) mIoU improvements across L_2 based mFGSM attack, (d) mIoU improvements using BPDA on L_∞ based mFGSM attack. **Note, in all plots the Wiener filter is based on L_∞ based attacks.**

sive improvement of +8% absolute on ICNet and 3.36% absolute on FCN, thereby indicating strong generalization towards unseen attacks. In comparison to other baselines, only NL means remains competitive, improving mIoU by an average 5.8% absolute on ICNet and only 0.61% absolute on FCN. All other baseline methods, in contrast to existing beliefs (Xu, Evans, and Qi 2018; Guo et al. 2018), offer only marginal improvements in our complex task setting. Additionally, we investigated various combinations of denoising methods, and found WF can easily be combined with other methods, with the best combination being WF (combined) + NL means. *Such a defense consistently beats all methods in every experiment we performed, however, at a downside of small performance drop on clean images.*

Generalization across L_p norms. In a real-world setting, an attacker can vary many things to alter his attack strategy. Hence, a defense strategy that works well under such mismatched conditions is highly desirable. We investigated the performance of all methods with the mFGSM attack on ICNet, computed using an L_2 norm ($\epsilon = 5000$). Note that the WF used here is still computed on the L_∞ norm instead. The results are shown in Fig. 5 (c). Even in this mismatched setting, WF outperforms all other methods, thereby highlighting the benefits of frequency-domain based denoising.

Generalization across white-box attacks (BPDA). Lastly, we investigate the performance of our model in a pure white-box setting using the BPDA attack algorithm

with the mFGSM attack as described in Sec. 4.2. Considering fixed parameter settings (L_∞ norm with $\epsilon = 10$) for each denoising method, the attack success is reported in Fig. 5 (d). In absolute performance after attack, WF (combined), *outperforms all other methods individual methods.* However, in terms of relative performance drop before and after BPDA, WF (combined) seems to be weaker than the other methods. Finally, we observe that WF+NLM seems to be the strongest defense under all attack variations and settings that we tried.

6 CONCLUSION

In this paper, we performed detailed frequency-domain analysis of adversarial images across four attack types on a complex task, namely semantic segmentation and report two key findings. First, we observed that *attacked images tend to exhibit artifacts/patterns in the frequency domain that are largely image- and attack-type independent.* Further investigations revealed that *these artifacts originate during the attack generation process while propagating gradients across different layers of the network.*

Motivated from these findings, we further proposed an adversarial defense method that suppresses these observed frequency patterns/artifacts using the well-known Wiener filters. Using our method, we beat five state-of-the-art adversarial denoising methods across different L_p norms in both gray-box and white-box attack settings. The generalization ability of WF can be largely attributed to the attack-agnostic

properties of the underlying frequency patterns. We hope to motivate researchers to investigate adversarial attacks further from a frequency domain perspective which might help in not only defending against unseen adversarial attacks but also in building robust architectures.

7 ACKNOWLEDGEMENT

The research leading to these results is funded by the German Federal Ministry for Economic Affairs and Energy within the project “KI Absicherung – Safe AI for Automated Driving”. The authors would like to thank the consortium for the successful cooperation.

8 Supplementary Material

8.1 Additional Details on Experimental Setup

We provide detailed descriptions of the adversarial attacks we considered, the baseline defense methods used for comparison and the corresponding metrics used to report our results.

Adversarial Attacks According to Assion *et al.* (Assion *et al.* 2019), an adversarial attack consists of solving a constrained optimization problem with the constraint being the strength of the perturbation itself, usually in the form of an L_p norm, mostly L_2 or L_∞ . Additionally depending on the attack input, an adversarial perturbation is usually computed in an iterative gradient based manner by repeated forward and backward passes through different layers of a CNN. An attack is said to be successful, if the optimization goal is reached within the permissible adversarial strength budget in a fixed number of iteration steps. These attacks are further classified depending on the optimization goal, adversary’s knowledge, etc. For the sake of consistency, we follow attack conventions proposed by Assion *et al.* (Assion *et al.* 2019). Additionally, we incorporated adversarial attacks from their framework `AidKit`² for the scope of this work. The reason for this is mainly because, unlike existing frameworks such as `Foolbox` (Rauber, Brendel, and Bethge 2017), `Cleverhans` (Papernot *et al.* 2018) etc., which primarily work on the image classification task, `AidKit` employs attacks directly on the complex semantic segmentation task.

In this work, we consider *two targeted* attacks, namely momentum FGSM (mFGSM) (Dong *et al.* 2018) and Metzen LLM (Metzen *et al.* 2017), *one untargeted* attack, namely Mopuri (Reddy, Ganeshan, and Babu 2018), which at the same time is an image-agnostic attack and *one confusion* based attack, namely iterative mirror (I.M.) (Metzen *et al.* 2017).

Targeted attacks A targeted adversarial attack aims at fooling a CNN, such that for a given class $s \in \mathcal{S}$, the predicted class $s_i^*(\mathbf{x})$ does not match with the ground truth class $s_i(\mathbf{x})$ at each pixel $i \in \mathcal{I}$ of the input image \mathbf{x} . We elaborate on the two targeted attacks used in this work as follows.

²<https://aidkit.ai/>

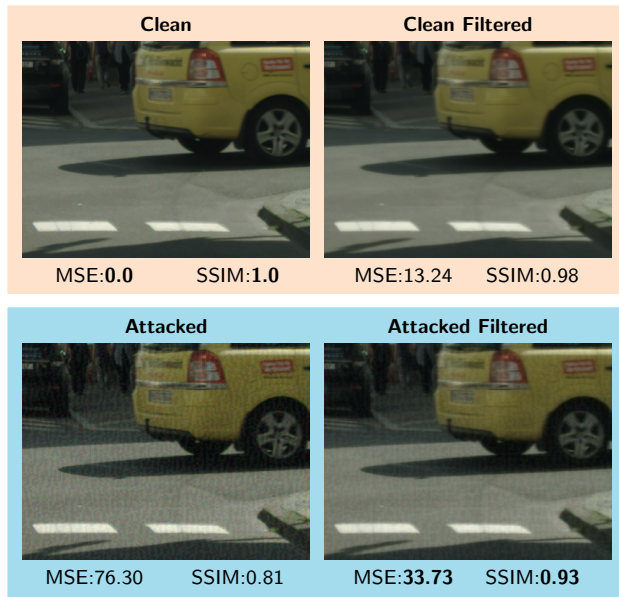


Figure 6: **Visualization of Wiener filtering on clean data and perturbed/attacked data.** An example image $\mathbf{x} \in \mathcal{X}^{\text{val}}$ is cropped and visualized to demonstrate the effect of denoising using a Wiener filter \mathcal{G} as shown in (6) for the Mopuri attack (Reddy, Ganeshan, and Babu 2018) with $\epsilon = 10$. Additionally, the MSE and the SSIM is reported with respect to the unfiltered clean data. It can be seen that Wiener filtering on clean data leads to an increase of MSE, but still keeps the SSIM at a reasonably high value. On the other hand, when being applied to perturbed/attacked data, the Wiener filtering successfully decreases the MSE, while at the same time it substantially increases the SSIM.

Momentum FGSM: Goodfellow *et al.* (Goodfellow, Shlens, and Szegedy 2015) originally proposed the fast gradient sign method (FGSM) which was later on extended to iterative FGSM by Kurakin *et al.* (Kurakin, Goodfellow, and Bengio 2017). Dong *et al.* (Dong *et al.* 2018) further boosted the iterative FGSM by integrating a momentum term into the iterative process, resulting in a much stronger and stable attack called momentum FGSM (mFGSM). We present the details of this attack next. Given set of input images \mathcal{X}' , imperceptibility constant $\epsilon > 0$ and $s \in \mathcal{S}$ as the index of the class (target) that the adversary wants to erase (e.g. pedestrian class), the mFGSM attack effectively tries to solve the following optimization problem

$$\min_{\mathbf{r}} \sum_{\mathbf{x} \in \mathcal{X}'} \|\mathbf{y}_s(\mathbf{x} + \mathbf{r})\|_2 \quad \text{s.t.} \quad \|\mathbf{r}\|_p \leq \epsilon, \quad (12)$$

where $\mathbf{y}_s = P(s|\mathbf{x})$ represents the output probability scores for target class s , given an input image \mathbf{x} and $\|\cdot\|_p$ represents an L_p norm. This optimization problem is solved in an iterative fashion as follows

$$\begin{aligned} \mathbf{x}_t^{\text{adv}} &= \mathbf{x}_{t-1}^{\text{adv}} + \mathbf{r}_t; \\ \mathbf{r}_t &= \mathbf{r}_{t-1} - \lambda \text{sign}(\mathbf{g}_t), \end{aligned} \quad (13)$$

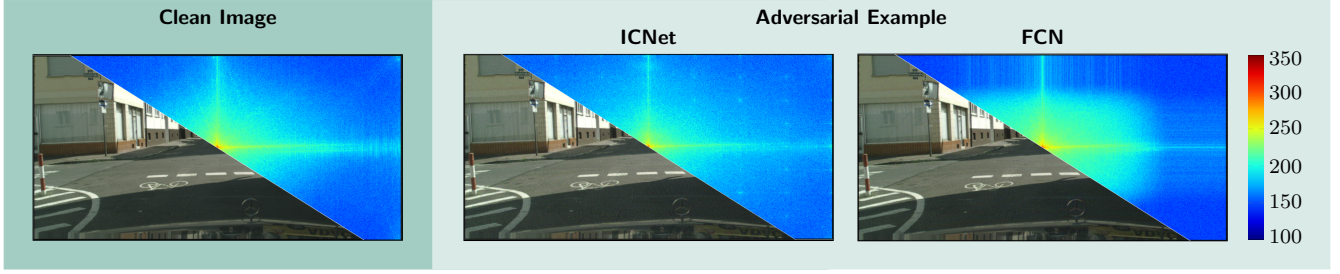


Figure 7: **Image frequency spectra comparison** of clean v/s attacked image.

where $t \in \{1, 2, \dots, T\}$ denotes the iteration step, $\lambda = \epsilon/T$ denotes the step size. Note that $\text{sign}(\cdot) \in \{\pm 1\}^{H \times W \times C}$. The perturbation \mathbf{r}_t is derived from the input gradient \mathbf{g}_t at iteration t as

$$\mathbf{g}_t = (1 + \mu \mathbf{g}_{t-1}) \sum_{j=1}^{|\mathcal{X}'|} \nabla_{\mathbf{x}} \|\mathbf{y}_s(\mathbf{x}_j + \mathbf{r}_{j-1})\|_2, \quad (14)$$

where μ denotes the momentum constant and \mathcal{X}' denotes the set of input images used to compute the attack, often referred to as scope. For individual scope, i.e. an attack computed for each image individually, only individual images are used, i.e. $|\mathcal{X}'| = 1$. The attack is initialized with $\mathbf{g}_0 = 0$, $\mathbf{r}_0 = 0$, and the output adversarial image is $\mathbf{x}^{\text{adv}} = \mathbf{x}_T^{\text{adv}}$. In this paper, we only consider attacks of *individual scope*.

Metzen LLM: Metzen *et al.* (Metzen et al. 2017) showed the existence of targeted, universal adversarial attacks for state-of-the-art semantic segmentation neural networks. To generate these perturbations, Metzen *et al.* tried to solve

$$\min_{\mathbf{r}} \sum_{\mathbf{x} \in \mathcal{X}'} J_{\text{CE}}(\mathbf{y}(\mathbf{x} + \mathbf{r}), \mathbf{y}^{\text{target}}(\mathbf{x})) \quad \text{s.t.} \quad \|\mathbf{r}\|_p \leq \epsilon, \quad (15)$$

where J_{CE} denotes the cross-entropy classification loss and $\mathbf{y}^{\text{target}}(\mathbf{x})$ denotes a fake segmentation output which is created beforehand such that pixels of a target class s are replaced by pixels of the nearest neighbor class following the minimum Euclidean distance calculation. This makes the fake segmentation output look more realistic when a target class s is removed. We refer the reader to (Metzen et al. 2017) for detailed formulations of $\mathbf{y}^{\text{target}}$. The optimization problem is solved in an iterative manner similar to (13), with the gradient \mathbf{g}_t being

$$\mathbf{g}_t = \lambda \text{sign}(\nabla_{\mathbf{x}} J_{\text{CE}}(\mathbf{y}(\mathbf{x} + \mathbf{r}), \mathbf{y}^{\text{target}}(\mathbf{x}))), \quad (16)$$

where $\mathbf{r}_0 = 0$ and $\mathbf{x}^{\text{adv}} = \mathbf{x}_T$. Technically, given such an attack formulation, an attacker can simply create any number of fake segmentation masks by manually designing $\mathbf{y}^{\text{target}}(\mathbf{x})$ beforehand and optimize the attack towards this attack and it would still be successful. We show how this could be done in the iterative mirror attack next.

Confusion-based attacks Although some attackers might target specific classes, adversarial attacks can also be created with an aim of causing confusion in the output. One example

of such an attack is presented by Assion *et al.* (Assion et al. 2019) in their framework `AidKit`, namely iterative mirror.

Iterative mirror: Inspired by the Metzen *et al.* attack, Assion *et al.* presented an alternative formulation of the target fake segmentation map $\mathbf{y}^{\text{target}}(\mathbf{x})$ such that the segmentation output looks like a mirror image, hence creating confusion. This is achieved by simply modifying the $\mathbf{y}^{\text{target}}(\mathbf{x})$ as follows

$$\mathbf{y}_{h,w}^{\text{target}}(\mathbf{x}) = \mathbf{y}(\mathbf{x})_{h,W-w}, \quad (17)$$

where h, w denote the pixel indices along height H and width W of an input image \mathbf{x} . This trick simply maps the pixels on the right to pixels on the left and vice versa in the output segmentation map. The rest of the optimization method is the same as shown in (15) and (16) which leads to a mirrored segmentation output.

Untargeted attacks An untargeted attack does not have a specific preference in a particular class of the output, but rather aims at as many misclassifications as possible.

Data-Free Mopuri: Mopuri *et al.* (Reddy, Ganeshan, and Babu 2018) proposed an universal adversarial attack that is image- and task-agnostic and generalizes across several architectures. The key idea is to optimize the attack such that the computed perturbation maximizes feature map activations $\mathbf{f}_{\ell}(\cdot)$ of a subset of layers $\ell \in \mathcal{L}$, thereby implying a lot of misclassifications. This is achieved by solving the following optimization problem

$$\min_{\mathbf{r}} -\log\left(\prod_{\ell \in \mathcal{L}} \|\mathbf{f}_{\ell}(\mathbf{r}_0 + \mathbf{r})\|_2\right) \quad \text{s.t.} \quad \|\mathbf{r}\|_p \leq \epsilon, \quad (18)$$

where $\mathbf{f}_{\ell}(\cdot)$ denotes the feature map activations of a layer $\ell \in \mathcal{L}$ and \mathbf{r}_0 is a randomly initialized perturbation at $t = 0$. The optimization problem is solved in an iterative way, similar to the Momentum FGSM attack as shown in (13) and (14), leading to a strong universal attack. Note that the optimization objective does not need any input clean images, hence it is *image-agnostic*. This attack also does not need to know anything about the output of the neural network, making it also a *task-agnostic* attack.

Baseline Defense Methods For the complex semantic segmentation task, we limit our investigations to adversarial defenses of type *input transformation*, specifically the ones that do not need additional retraining. This is done to avoid

additional computational overhead. We investigate two well-known categories of such defenses, namely image compression (Dziugaite, Ghahramani, and Roy 2016) and feature squeezing (Xu, Evans, and Qi 2018) methods. We present details of both these methods next.

Image Compression Image compression is a well known technique of reducing redundancy in an image in an efficient form. As an adversarial defense, JPEG compression and JPEG 2000 compression are well-known.

JPEG compression was first proposed by Dziugaite *et al.* (Dziugaite, Ghahramani, and Roy 2016) and further investigated in (Aydemir, Temizel, and Temizel 2018; Shaham *et al.* 2018; Prakash *et al.* 2018). JPEG compression is mainly a lossy compression method that first transforms an image into 8×8 blocks and converts them to frequencies using the discrete cosine transform (DCT). Next, in order to reduce redundancy, it suppresses high frequencies using quantization, thereby introducing unwanted blocking artifacts, specifically at high compression rates.

JPEG 2000 compression was proposed by Aydemir *et al.* (Aydemir, Temizel, and Temizel 2018) in order to alleviate the shortcomings of JPEG compression. As JPEG 2000 uses wavelet transforms over DCT, and does not need image transformation into blocks, blocking artifacts are thereby not introduced, even at high compression rates. However, Aydemir *et al.* concluded that a good quality or lossless compression does not necessarily mean a good defense, as it also tends to unknowingly preserve the adversarial perturbations.

Feature Squeezing Xu *et al.* (Xu, Evans, and Qi 2018) introduced feature squeezing as a bunch of techniques that aim at reducing the input space features, thereby reducing the available search space for an adversary. Although there are many such methods possible, they explored bit-depth reduction and spatial smoothing techniques. These methods are, however, proposed from an adversarial detector perspective.

Median Blurring (MB) (Aydemir, Temizel, and Temizel 2018) is a type of local *spatial smoothing* method widely known in image processing to reduce noise. A median filter is applied locally where each pixel is replaced with the median of a few of its neighboring pixels. Similarly, one can also perform mean or Gaussian smoothing.

Non-Local Smoothing (NLM) In contrast, *non-local smoothing* algorithm utilizes much larger areas of the image for smoothing instead of just neighboring pixels. More specifically, in NLM (Buades, Coll, and Morel 2005), every pixel is replaced by a weighted average of all other pixels in the image where the weightage is computed based on how similar each pixel is to the target pixel.

Bit-Depth Reduction An 8-bit grayscale image corresponds to $2^8 = 256$ available colors. In contrast, an 8-bit RGB image corresponds to 24 bits per pixel (8 bits per channel), and therefore $2^{24} \approx 16$ million colors. While most humans can recognize black and white images just as good as color images, it is often hypothesized that reducing the number of available color bits might not harm the classification performance as such and thereby also reduce the search

space for an adversary.

Evaluation Metrics Our results are reported on the following metrics:

Mean Squared Error (MSE) We compute the mean squared error between the attacked image \mathbf{x}^{adv} and the attacked denoised image $\hat{\mathbf{x}}$ by

$$MSE(\mathbf{x}^{\text{adv}}, \hat{\mathbf{x}}) = \frac{1}{HWC} \sum_{h=0}^{H-1} \sum_{w=0}^{W-1} \sum_{c=0}^{C-1} (x_{h,w,c}^{\text{adv}} - \hat{x}_{h,w,c})^2, \quad (19)$$

where h, w, c denote the indices of the images along height, width and channels, respectively. Additionally, we also compute the MSE between the clean image \mathbf{x} as well as its clean filtered image \mathbf{x}' which is computed by $\mathbf{x}' = \mathcal{F}^{-1}(\mathbf{X}')$ where

$$\mathbf{X}' = \mathbf{G} \odot \mathbf{X}. \quad (20)$$

Structural Similarity Metric (SSIM) We also compute the structural similarity index metric (SSIM) according to (Wang *et al.* 2004) on the attacked image \mathbf{x}^{adv} and the attacked denoised image $\hat{\mathbf{x}}$ as follows

$$SSIM(\mathbf{x}^{\text{adv}}, \hat{\mathbf{x}}) = [l(\mathbf{x}^{\text{adv}}, \hat{\mathbf{x}})]^\alpha \cdot [c(\mathbf{x}^{\text{adv}}, \hat{\mathbf{x}})]^\beta \cdot [s(\mathbf{x}^{\text{adv}}, \hat{\mathbf{x}})]^\gamma, \quad (21)$$

where $l(\cdot, \cdot), c(\cdot, \cdot), s(\cdot, \cdot)$ are mathematical functions denoting a measure of luminosity, contrast, and saturation, respectively, and α, β, γ are weighting constants. We refer the reader to (Wang *et al.* 2004) for detailed definitions of these functions. The SSIM values range from 0 (lowest) to 1 (highest). Similarly we also report results on SSIM between the clean image \mathbf{x} and the clean filtered image \mathbf{x}' .

Mean Intersection over Union (mIoU) : For semantic segmentation, *mean intersection-over-union* (mIoU) is commonly used to evaluate the performance of the network. It is computed by

$$mIoU = \frac{1}{|\mathcal{S}|} \sum_{s \in \mathcal{S}} \frac{TP(s)}{TP(s) + FP(s) + FN(s)}, \quad (22)$$

where $TP(s), FP(s), FN(s)$ indicate class specific true positives, false positives and false negatives respectively.

8.2 Additional Results

In Fig. 6, we show qualitatively the denoising influence of using Wiener filters on a sample example image computed from the Cityscapes validation set. Both metrics MSE and SSIM show favorable results after denoising on clean and attacked images.

Fourier Domain Analysis Additionally to the paper, we provide further results of Fourier analysis of adversarial examples, as well as detailed results of Wiener filtering as a defense for segmentation. In Fig. 7, we demonstrate the DFT spectrum of a single clean and corresponding attacked image on the ICNet and the FCN model. Clear grid-shaped and

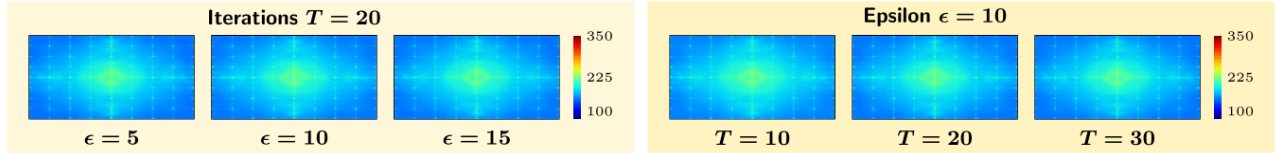


Figure 8: Average DFT of adversarial perturbations varied along attack parameters: attack strength ϵ , and total number of iterations T .

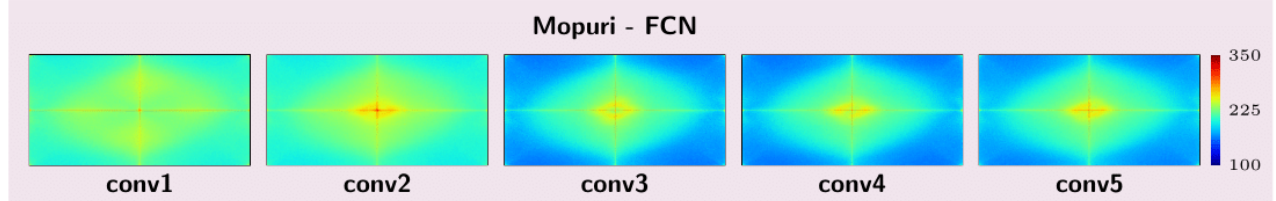


Figure 9: Average DFT of adversarial perturbations for Mopuri attack on FCN varied along attacked layer ℓ .

Table 3: **Comparison of SSIM and MSE metrics** with and without denoising for the ICNet (Zhao et al. 2018) model trained on the Cityscapes dataset. We report averaged SSIM and MSE performance over the entire **validation set** images w.r.t. the reference clean images x of (a) the **attacked** images x^{adv} **across all attacks** with strength $\epsilon = 10$ based on the L_∞ **norm**, (b) the corresponding **attacked denoised** images \hat{x} , and (c) the **clean filtered** images x' . In the case of Wiener filtering, the filters are computed over clean and adversarial images with strength $\epsilon = 5$ (**unmatched** conditions) and $\epsilon = 10$ (**matched** conditions) spanning the entire training set. An increase in SSIM after denoising, and a corresponding decrease in MSE are desired. The best denoised results are marked in **bold**, second best underlined, with the Wiener upper limit and single-attack Wiener filters $G^{(a)}$, $G^{(\text{Metzen.Ped})}$, $G^{(\text{mFGSM.Car})}$ being excluded. The values in Fig. 5(a) of the paper are taken from the **Attacked Denoised** column of this table.

Method		Average SSIM			Average MSE		
		Attacked	Attacked Denoised	Clean Filtered	Attacked	Attacked Denoised	Clean Filtered
Wiener (Ours)	G (upper limit)		0.95	1.00		47.80	0.00
	$G^{(a)}$ matched	0.89	0.95	0.99	78.76	57.20	14.07
	$G^{(a)}$ unmatched		0.93	1.00		<u>56.04</u>	5.12
	$G^{(\text{Metzen.Ped})}$ matched		0.92	1.00		59.11	4.38
	$G^{(\text{Metzen.Ped})}$ unmatched		0.91	1.00		62.54	2.23
	$G^{(\text{mFGSM.Car})}$ matched		<u>0.94</u>	0.98		65.96	23.99
	$G^{(\text{mFGSM.Car})}$ unmatched		0.93	0.99		58.19	8.47
$G^{(A)}$ matched	<u>0.94</u>		0.99	59.18		11.38	
$G^{(A)}$ unmatched	0.92	1.00	59.25	4.28			
JPEG compression			0.90	0.98		82.50	13.92
JPEG 2000 compression			0.89	1.00		80.42	0.00
NL Means			0.92	0.98		60.71	8.61
Median Blur			0.90	0.98		84.20	16.17
Bit Depth Reduction			0.86	0.95		86.87	17.48
Wiener $G^{(A)}$ (matched) + NL Means			<u>0.94</u>	0.97		57.03	23.74
Wiener $G^{(A)}$ (unmatched) + NL Means			<u>0.94</u>	0.97		51.76	15.61

box-shaped artifacts are observed for both attacked images (as also summarized in the paper).

In Fig. 8, we demonstrate results of our ablation study on the effect of varying attack parameters, namely epsilon ϵ and number of iterations T . These results are reported for the

attack on the ICNet model using an L_∞ norm. From this, we can conclude that the artifacts are largely independent to attack strength and the number of iterations used for the attack generation.

Lastly, in Fig. 9, we show the results of varying layers ℓ

Table 4: **Comparison of mIoU (in %)** with and without denoising for the ICNet (Zhao et al. 2018) model trained on the Cityscapes dataset. We report the mIoU w.r.t. the reference clean images x of (a) the **attacked** images x^{adv} , (b) the **attacked denoised** images \hat{x} , and (c) the **clean filtered** images x' over the entire **validation set** $\mathcal{D}_{\text{CS}}^{\text{val}}$ with adversarial examples ($\epsilon = 10$ based on L_∞ norm). In the case of Wiener filtering, the filters are computed over clean and adversarial images with strength $\epsilon = 5$ (**unmatched** conditions) and $\epsilon = 10$ (**matched** conditions) spanning the entire training set. Best results are shown in **bold**, second best underlined with the Wiener upper limit being excluded. The values in Fig. 5(c) are taken from the right-most column of this table.

Method		none (clean)	mFGSM (Car)	mFGSM (Ped)	Metzen (Car)	Metzen (Ped)	I.M.	Mopuri	All attacks (mean)		
Baseline mIoU (%)		67.25	20.23	20.39	64.61	65.73	42.87	27.65	40.24		
mIoU (%) Denoised	Wiener (Ours)	G (upper limit)	67.25	35.97	36.53	65.77	66.49	50.31	41.27	49.39	
		$G^{(a)}$	matched	66.43	<u>32.53</u>	33.05	65.48	66.22	46.60	<u>38.96</u>	47.14
			unmatched	67.03	28.37	28.73	65.14	66.03	44.67	33.75	44.45
		$G^{(\text{Metzen.Ped})}$	matched	67.12	24.98	25.14	65.47	66.22	46.29	31.20	43.22
			unmatched	<u>67.18</u>	22.75	22.91	65.13	66.03	44.44	29.54	41.80
		$G^{(\text{mFGSM.Car})}$	matched	65.54	<u>32.53</u>	<u>33.18</u>	66.07	66.07	53.75	37.37	48.16
			unmatched	66.85	28.37	28.75	65.84	66.39	49.41	34.16	45.49
		$G^{(A)}$	matched	66.76	28.82	29.14	65.94	66.38	49.98	35.02	45.88
			unmatched	67.07	25.43	25.60	65.51	66.26	46.70	31.80	43.55
		JPEG Compression		66.99	20.27	20.05	65.03	65.80	46.72	27.94	40.96
		JPEG 2000 compression		67.25	20.12	20.25	64.61	65.73	42.87	27.52	40.18
		NL Means		65.50	27.20	27.49	66.45	66.48	55.20	33.44	46.04
		Median Blur		67.05	21.59	20.98	65.64	66.47	47.64	28.41	41.78
		Bit Depth Reduction		62.07	19.77	19.77	62.24	62.88	45.87	26.80	39.55
		Wiener $G^{(A)}$ (matched) + NL Means		65.18	35.87	37.07	<u>66.46</u>	<u>66.49</u>	59.65	41.65	51.19
Wiener $G^{(A)}$ (unmatched) + NL Means		65.47	32.22	32.93	66.83	66.93	<u>57.95</u>	38.44	<u>49.21</u>		

Table 5: **Comparison of mIoU (in %)** with and without denoising for the FCN model trained on the Cityscapes dataset. We report the mIoU w.r.t. the reference clean images x of (a) the **attacked** images x^{adv} , (b) the **attacked denoised** images \hat{x} , and (c) the **clean filtered** images x' over the entire **validation set** with adversarial examples ($\epsilon = 10$ for mFGSM and Mopuri; and $\epsilon = 40$ for Iterative Mirror and Metzen attacks, both based on L_∞ norm). In the case of Wiener filtering, the filters are computed over clean and adversarial images with strength $\epsilon = 10, 40$ (**matched** conditions) spanning the entire training set $\mathcal{D}_{\text{DS}}^{\text{train}}$. Best results are shown in **bold**, second best underlined with the Wiener upper limit being excluded. The values in Fig. 5(c) of the paper are taken from the right-most column of this table.

Method		none (clean)	mFGSM (Car)	mFGSM (Ped)	Metzen (Car)	Metzen (Ped)	I.M.	Mopuri	All attacks (mean)		
Baseline mIoU (%)		48.48	20.97	20.65	28.30	31.39	19.77	30.42	28.56		
mIoU (%) Denoised	Wiener (Ours)	G (upper limit)	48.48	29.84	29.86	36.75	38.92	31.42	37.81	36.15	
		$G^{(a)}$	matched	48.15	<u>27.93</u>	<u>27.60</u>	<u>34.99</u>	37.33	<u>27.89</u>	<u>37.28</u>	<u>32.17</u>
			unmatched	48.28	27.25	26.95	<u>34.99</u>	37.33	27.60	34.92	31.50
		$G^{(\text{Metzen.Car})}$	matched	48.12	<u>27.93</u>	<u>27.60</u>	34.95	<u>37.38</u>	27.84	35.85	31.92
			unmatched	48.21	27.52	27.38	<u>34.99</u>	37.26	27.56	35.87	31.76
		$G^{(A)}$		48.21	27.52	27.38	<u>34.99</u>	37.26	27.56	35.87	31.76
		JPEG Compression		48.09	23.30	23.06	30.98	34.18	23.04	31.64	27.70
		JPEG 2000 compression		48.48	23.06	22.99	30.57	33.84	22.19	31.89	27.41
		NL Means		48.03	24.62	24.64	32.44	35.67	24.47	33.26	29.17
		Median Blur		<u>48.42</u>	23.46	23.49	31.66	34.92	23.52	32.11	28.19
		Bit Depth Reduction		46.39	22.86	22.76	30.82	33.99	22.63	31.27	27.38
		Wiener $G^{(A)}$ + NL Means		47.78	29.60	29.33	37.36	39.12	30.59	37.08	33.84

in the Mopuri attack computed on the FCN model, instead of ICNet (as shown in Fig. 4 in the paper). Since the FCN architecture consists pre-dominantly of down sampling layers, the corresponding differences in the resulting artifacts is relatively smaller as in the multi-stream architecture of the ICNet. We leave a detailed study of the effect of individual layer types (found commonly in CNNs) on the resulting artifacts to future study.

Wiener filters as an Adversarial Defense We provide detailed results on the effectiveness of using Wiener filters as an adversarial defense. Please note that the results shown in Fig. 5 (a) and 5 (c) of the paper are adapted/summarized from the tables presented here.

SSIM and MSE Results The effect of Wiener filter based denoising in comparison to existing methods on traditional metrics such as MSE and SSIM are reported in Tab. 3. In the paper, we only reported the final aggregated summary, however detailed results are presented here. Additionally, different combinations (epsilon and attack mismatch between creation and evaluation of Wiener filter) of Wiener filters are also reported here. Essentially, more or less every combination of Wiener filter that we tried beat all the remaining state of the art denoising methods on both SSIM as well as MSE.

mIoU Results The results of Fig. 5 (c) in the paper are adapted from the right-most column of Tab. 4 and Tab. 5. Additionally, as before, we present additional results of different variants of Wiener filters with an epsilon and attack mismatch. From these results, we can conclude that Wiener filters tend to work well under various mismatched conditions, which is better than other methods. The reason for their success can be attributed directly to their frequency-based denoising nature since the artifacts they try to suppress remain more or less the same (see Fig. 8) even under various mismatched conditions.

References

- Assion, F.; Schlicht, P.; Greßner, F.; Gunthe, W.; Hüger, F.; Schmidt, N.; and Rasheed, U. 2019. The Attack Generator: A Systematic Approach Towards Constructing Adversarial Attacks. In *Proc. of CVPR - SAIAD Workshop*, 1370–1379. Long Beach, CA, USA.
- Athalye, A.; Carlini, N.; and Wagner, D. 2018. Obfuscated Gradients Give a False Sense of Security: Circumventing Defenses to Adversarial Examples. In *Proc. of ICML*, 274–283. Stockholm, Sweden.
- Aydemir, A. E.; Temizel, A.; and Temizel, T. T. 2018. The Effects of JPEG and JPEG2000 Compression on Attacks Using Adversarial Examples. *arXiv* (1803.10418).
- Buades, A.; Coll, B.; and Morel, J.-M. 2005. A Non-Local Algorithm for Image Denoising. In *Proc. of CVPR*. San Diego, CA, USA.
- Burger, W.; and Burge, M. J. 2008. *Principles of Digital Image Processing*. Springer.
- Bär, A.; Hüger, F.; Schlicht, P.; and Fingscheidt, T. 2019. On the Robustness of Teacher-Student Frameworks for Semantic Segmentation. In *Proc. of CVPR - Workshops*, 1380–1388. Long Beach, CA, USA.
- Bär, A.; Klingner, M. R.; Varghese, S.; Hüger, F.; Schlicht, P.; and Fingscheidt, T. 2020. Robust Semantic Segmentation by Redundant Networks With a Layer-Specific Loss Contribution and Majority Vote. In *Proc. of CVPR - SAIAD Workshop*, 1348–1358. Seattle, WA, USA.
- Chakraborty, A.; Alam, M.; Dey, V.; Chattopadhyay, A.; and Mukhopadhyay, D. 2018. Adversarial Attacks and Defences: A Survey. *arXiv* (1810.00069).
- Chen, J.; Wua, X.; Rastogi, V.; Liang, Y.; and Jha, S. 2018. Towards Understanding Limitations of Pixel Discretization Against Adversarial Attacks. *arXiv* (1805.07816).
- Chen, L.-C.; Papandreou, G.; Kokkinos, I.; Murphy, K.; and Yuille, A. L. 2015. Semantic Image Segmentation With Deep Convolutional Nets and Fully Connected CRFs. In *Proc. of ICLR*, 834–848. San Diego, CA, USA.
- Chen, L.-C.; Papandreou, G.; Schroff, F.; and Adam, H. 2017. Rethinking Atrous Convolution for Semantic Image Segmentation. *arXiv* (1706.05587).
- Cisse, M.; Bojanowski, P.; Grave, E.; Dauphin, Y.; and Usunier, N. 2017. Parseval Networks: Improving Robustness to Adversarial Examples. In *Proc. of ICML*, 854–863. Sydney, Australia.
- Cohen, J. M.; Rosenfeld, E.; and Kolter, J. Z. 2019. Certified Adversarial Robustness via Randomized Smoothing. In *Proc. of ICML*, 1310–1320. Long Beach, CA, USA.
- Cordts, M.; Omran, M.; Ramos, S.; Rehfeld, T.; Enzweiler, M.; Benenson, R.; Franke, U.; Roth, S.; and Schiele, B. 2016. The Cityscapes Dataset for Semantic Urban Scene Understanding. In *Proc. of CVPR*, 3213–3223. Las Vegas, NV, USA.
- Das, N.; Shanbhogue, M.; Chen, S.-T.; Hohman, F.; Li, S.; Chen, L.; Kounavis, M. E.; and Chau, D. H. 2018. Shield: Fast, Practical Defense and Vaccination for Deep Learning using JPEG Compression. In *Proc. of KDD*. London, UK.
- Demontis, A.; Melis, M.; Pintor, M.; Jagielski, M.; Biggio, B.; Oprea, A.; Nita-Rotaru, C.; and Roli, F. 2019. Why Do Adversarial Attacks Transfer? Explaining Transferability of Evasion and Poisoning Attacks. In *Proc. of SEC*, 321–338. Santa Clara, CA, USA.
- Dong, Y.; Liao, F.; Pang, T.; Su, H.; Zhu, J.; Hu, X.; and Li, J. 2018. Boosting Adversarial Attacks With Momentum. In *Proc. of CVPR*, 9185–9193. Salt Lake City, UT, USA.
- Dziugaite, G. K.; Ghahramani, Z.; and Roy, D. M. 2016. A Study of the Effect of JPEG Compression on Adversarial Images. *arXiv* (1608.00853).
- Fingscheidt, T.; Suhadi, S.; and Stan, S. 2008. Environment-Optimized Speech Enhancement. *IEEE TASLP* 16(4): 825–834.
- Frank, J.; Eisenhofer, T.; Schönherr, L.; Fischer, A.; Kolossa, D.; and Holz, T. 2020. Leveraging Frequency Analysis for Deep Fake Image Recognition. In *Proc. of ICML*, 214–223. Vienna, Austria.
- Gazi, O. 2018. *Understanding Digital Signal Processing*. Springer.
- Gonzalez, R. C.; and Woods, R. E. 2002. *Digital Image Processing*. Prentice Hall.
- Goodfellow, I. J.; Shlens, J.; and Szegedy, C. 2015. Explaining and Harnessing Adversarial Examples. In *Proc. of ICLR*. San Diego, CA, USA.

- Graese, A.; Rozsa, A.; and Boulton, T. E. 2016. Assessing Threat of Adversarial Examples on Deep Neural Networks. In *Proc. of IEEE ICMLA*, 69–74. Anaheim, CA, USA.
- Guo, C.; Rana, M.; Cisse, M.; and van der Maaten, L. 2018. Countering Adversarial Images Using Input Transformations. In *Proc. of ICLR*. Vancouver, Canada.
- Kannan, H.; Kurakin, A.; and Goodfellow, I. 2018. Adversarial Logit Pairing. *arXiv* (1803.06373).
- Kazubek, M. 2003. Wavelet Domain Image De-noising by Thresholding and Wiener Filtering. *IEEE Signal Processing Letters* 10(11): 324–326.
- Kethwas, A.; and Jharia, B. 2015. Image Denoising Using Fuzzy and Wiener Filter in Wavelet Domain. In *Proc. of ICECCT*. Coimbatore, TN, India.
- Klingner, M. R.; Bär, A.; and Fingscheidt, T. 2020. Improved Noise and Attack Robustness for Semantic Segmentation by Using Multi-Task Training with Self-Supervised Depth Estimation. In *Proc. of CVPR - SAIAD Workshop*, 1299–1309. Seattle, WA, USA.
- Krizhevsky, A.; Sutskever, I.; and Hinton, G. E. 2012. ImageNet Classification With Deep Convolutional Neural Networks. In *Proc. of NIPS*, 1097–1105. Lake Tahoe, USA.
- Kurakin, A.; Goodfellow, I.; and Bengio, S. 2017. Adversarial Machine Learning at Scale. In *Proc. of ICLR*. Toulon, France.
- Liao, F.; Liang, M.; Dong, Y.; Pang, T.; Hu, X.; and Zhu, J. 2018. Defense Against Adversarial Attacks Using High-Level Representation Guided Denoiser. In *Proc. of CVPR*, 1778–1787. Salt Lake City, UT, USA.
- Löhdefink, J.; Bär, A.; Schmidt, N. M.; Hüger, F.; Schlicht, P.; and Fingscheidt, T. 2019. On Low-Bitrate Image Compression for Distributed Automotive Perception: Higher Peak SNR Does Not Mean Better Semantic Segmentation. In *Proc. of IV*, 352–359. Paris, France.
- Long, J.; Shelhamer, E.; and Darrell, T. 2015. Fully Convolutional Networks for Semantic Segmentation. In *Proc. of CVPR*, 3431–3440. Boston, MA, USA.
- Lyons, R. G.; and Fugal, D. L. 2014. *The Essential Guide to Digital Signal Processing*. Prentice Hall.
- Madry, A.; Makelov, A.; Schmidt, L.; Tsipras, D.; and Vladu, A. 2018. Towards Deep Learning Models Resistant to Adversarial Attacks. In *Proc. of ICLR*. Vancouver, BC, Canada.
- Metzen, J. H.; Kumar, M. C.; Brox, T.; and Fischer, V. 2017. Universal Adversarial Perturbations Against Semantic Image Segmentation. In *Proc. of ICCV*, 2774–2783. Venice, Italy.
- Meyer, P.; Elshamy, S.; and Fingscheidt, T. 2020. A Multichannel Kalman-Based Wiener Filter Approach for Speaker Interference Reduction in Meetings. In *Proc. of ICASSP*, 451–455. Barcelona, Spain.
- Nguyen, A.; Yosinski, J.; and Clune, J. 2015. Deep Neural Networks Are Easily Fooled: High Confidence Predictions for Unrecognizable Images. In *Proc. of CVPR*, 427–436. Boston, MA, USA.
- Odena, A.; Dumoulin, V.; and Olah, C. 2016. Deconvolution and Checkerboard Artifacts. *Distill* URL <http://distill.pub/2016/deconv-checkerboard/>.
- Papernot, N.; Faghri, F.; Carlini, N.; Goodfellow, I.; Feinman, R.; Kurakin, A.; Xie, C.; Sharma, Y.; Brown, T.; Roy, A.; Matyasko, A.; Behzadan, V.; Hambardzumyan, K.; Zhang, Z.; Juang, Y.-L.; Li, Z.; Sheatsley, R.; Garg, A.; Uesato, J.; Gierke, W.; Dong, Y.; Berthelot, D.; Hendricks, P.; Rauber, J.; and Long, R. 2018. Technical Report on the CleverHans v2.1.0 Adversarial Examples Library. *arXiv preprint arXiv:1610.00768*.
- Papernot, N.; McDaniel, P.; Goodfellow, I.; Jha, S.; Celik, Z. B.; and Swamid, A. 2017. Practical Black-Box Attacks Against Machine Learning. In *Proc. of ASIA CCS*, 506–519. Abu Dhabi, UAE.
- Papernot, N.; McDaniel, P.; Wu, X.; Jha, S.; and Swami, A. 2015. Distillation as a Defense to Adversarial Perturbations Against Deep Neural Networks. *arXiv* (1511.04508).
- Papernot, N.; McDaniel, P.; Wu, X.; Jha, S.; and Swami, A. 2016. Distillation as a Defense to Adversarial Perturbations Against Deep Neural Networks. In *Proc. of IEEE Symposium on Security and Privacy (SP)*, 582–597. San Jose, CA, USA.
- Petrou, M.; and Petrou, C. 2010. *Image Processing: The Fundamentals*. Wiley.
- Prakash, A.; Moran, N.; Garber, S.; DiLillo, A.; and Storer, J. 2018. Deflecting Adversarial Attacks With Pixel Deflection. In *Proc. of CVPR*, 8571–8580. Salt Lake City, UT, USA.
- Raff, E.; Sylvester, J.; Forsyth, S.; and McLean, M. 2019. Barrage of Random Transforms for Adversarially Robust Defense. In *Proc. of CVPR*, 6521–6530. Long Beach, CA, USA.
- Raju, R.; and Lipasti, M. 2019. BlurNet: Defense by Filtering the Feature Maps. *arXiv* (1908.02256).
- Rauber, J.; Brendel, W.; and Bethge, M. 2017. Foolbox: A Python Toolbox to Benchmark the Robustness of Machine Learning Models. In *Proc. of ICML - Workshop*. URL <http://arxiv.org/abs/1707.04131>.
- Reddy, M. K.; Ganeshan, A.; and Babu, R. V. 2018. Generalizable Data-free Objective for Crafting Universal Adversarial Perturbations. *IEEE TPAMI* 41(10): 2452 – 2465.
- Scalart, P.; and Filho, J. 1996. Speech Enhancement Based on A Priori Signal to Noise Estimation. In *Proc. of ICASSP*, 629–632. Atlanta, GA, USA.
- Shaham, U.; Garritano, J.; Yamada, Y.; Weinberger, E.; Cloninger, A.; Cheng, X.; Stanton, K.; and Kluger, Y. 2018. Defending Against Adversarial Images Using Basis Functions Transformations. *arXiv* (1803.10840).
- Smith, S. W. 2003. *Digital Signal Processing - A Practical Guide for Engineers and Scientists*. Elsevier.
- Suhadi, S.; Last, C.; and Fingscheidt, T. 2011. A Data-Driven Approach to A Priori SNR Estimation. *IEEE TASLP* 19(1): 186–195.
- Szegedy, C.; Zaremba, W.; Sutskever, I.; Bruna, J.; Erhan, D.; Goodfellow, I.; and Fergus, R. 2014. Intriguing Properties of Neural Networks. In *Proc. of ICLR*. Montréal, QC, Canada.
- Tang, C.; Fan, Y.; and Yezzi, A. 2019. An Adaptive View of Adversarial Robustness from Test-time Smoothing Defense. In *Proc. of NIPS - Workshop*. Vancouver, Canada.
- Wang, H.; Wu, X.; Huang, Z.; and Xing, E. P. 2020a. High-frequency Component Helps Explain the Generalization of Convolutional Neural Networks. In *Proc. of CVPR*. Seattle, WA, USA.
- Wang, S.-Y.; Wang, O.; Zhang, R.; Owens, A.; and Efros, A. A. 2020b. CNN-generated images are surprisingly easy to spot...for now. In *Proc. of CVPR*, 8695–8704.
- Wang, Z.; Bovik, A.; Sheikh, H.; and Simoncelli, E. 2004. Image Quality Assessment: From Error Visibility to Structural Similarity. *IEEE Transactions on Image Processing* 13(4): 600–612.

- Wang, Z.; Yang, Y.; Shrivastava, A.; Rawal, V.; and Ding, Z. 2018. Towards Frequency-Based Explanation for Robust CNN. *arXiv* (1801.09344).
- Wiener, N. 1949. *Extrapolation, Interpolation, and Smoothing of Stationary Time Series*. MIT Press.
- Xie, C.; Wang, J.; Zhang, Z.; Ren, Z.; and Yuille, A. 2018. Mitigating Adversarial Effects Through Randomization. In *Proc. of ICLR*. Vancouver, Canada.
- Xu, W.; Evans, D.; and Qi, Y. 2018. Feature Squeezing: Detecting Adversarial Examples in Deep Neural Networks. In *Proc. of NDSS Symposium*. San Diego, USA.
- Yang, H. Z. 2017. TensorFlow Implementation of ICNet. <https://github.com/hellochick/ICNet-tensorflow>. Accessed: 2020-06-02.
- Yin, D.; Lopes, R. G.; Shlens, J.; Cubuk, E. D.; and Gilmer, J. 2019. A Fourier Perspective on Model Robustness in Computer Vision. In *Proc. of NIPS*, 13255–13265. Vancouver, Canada.
- Yu, F.; and Koltun, V. 2016. Multi-Scale Context Aggregation by Dilated Convolutions. In *Proc. of ICLR*. San Juan, Puerto Rico.
- Zhang, J.; Ding, Z.; Li, W.; and Ogunbona, P. 2018. Importance Weighted Adversarial Nets for Partial Domain Adaptation. In *Proc. of CVPR*, 8156–8164. Salt Lake City, UT, USA.
- Zhao, H.; Qi, X.; Shen, X.; Shi, J.; and Jia, J. 2018. ICNet for Real-Time Semantic Segmentation on High-Resolution Images. In *Proc. of ECCV*, 405–420. Munich, Germany.